

Cross-Domain Offshore Wind Power Forecasting: Transfer Learning Through Meteorological Clusters

Dominic Weisser¹, Chloé Hashimoto-Cullen² and Benjamin Guedj^{1,3}

¹University College London, United Kingdom.

²Sorbonne Université, France.

³Inria, France.

Keywords: transfer learning, wind power forecasting, Gaussian Processes

Abstract

Ambitious decarbonisation targets are catalysing growth in orders of new offshore wind farms. For these newly commissioned plants to run, accurate power forecasts are needed from the onset. These allow grid stability, good reserve management and efficient energy trading. Despite machine learning models having strong performances, they tend to require large volumes of site-specific data that new farms do not yet have. To overcome this data scarcity, we propose a novel transfer learning framework that clusters power output according to covariate meteorological features. Rather than training a single, general-purpose model, we thus forecast with an ensemble of expert models, each trained on a cluster. As these pre-trained models each specialise in a distinct weather pattern, they adapt efficiently to new sites and capture transferable, climate-dependent dynamics. Through the expert models' built-in calibration to seasonal and meteorological variability, we remove the industry-standard requirement of local measurements over a year. Our contributions are two-fold — we propose this novel framework and comprehensively evaluate it on eight offshore wind farms, achieving accurate cross-domain forecasting with under five months of site-specific data. Our experiments achieve a MAE of 3.52%, providing empirical verification that reliable forecasts do not require a full annual cycle. Beyond power forecasting, this climate-aware transfer learning method opens new opportunities for offshore wind applications such as early-stage wind resource assessment, where reducing data requirements can significantly accelerate project development whilst effectively mitigating its inherent risks.

Impact Statement

This work proposes a novel transfer learning pipeline for accurate offshore wind power forecasting that does not require the industry-standard of a full year of local measurements. Results demonstrate that early-stage uncertainty and costs can effectively be reduced, avoiding delays to project development and grid integration.

1. Introduction

Offshore wind power is tapped to be the cornerstone of the green energy transition, with global offshore wind capacity projected to triple from 83 GW in 2024 to 238 GW by 2030 (Ember Energy 2025). However, current wind farms are concentrated in a small number of developed countries (Statista 2025). This leaves many emerging market countries unexploited, with an estimated potential of 3.1 TW of offshore wind power between Brazil, India, Morocco, the Philippines, South Africa and Vietnam (ESMAP 2019). Of these, Vietnam is currently the only one with offshore wind farms (Global Wind Energy Council 2025).

To exploit these markets, both efficient Wind Resource Assessment (WRA) and accurate Wind Power Forecasting (WPF) from the start of operations are needed. In nascent markets with the highest uncertainty, reliable WPF is crucial to integrating intermittent generation into local grids, as it provides system stability, limits reserve requirements and hedges financial risks.

Traditional physical models for WPF are robust but computationally intensive and have systematic biases linked to the limited resolution of sub-grid-scale atmospheric processes. Thus, statistical and machine learning approaches have gained in prominence. Among these, deep learning approaches have state-of-the-art (SOTA) performance in offshore WPF (Ally et al 2025), in particular due to their abilities to model high-dimensional dependencies. Given the data-intensive nature of these models, current SOTA forecasting models are trained on granular, site-specific SCADA data accumulated over the years. The need for comprehensive local data limits performance for newly commissioned sites, particularly in emerging markets where data is scarce. Transfer learning is therefore emerging as an approach to leverage existing knowledge from a data-rich source domain \mathcal{D}_S to a data-scarce target domain \mathcal{D}_T (Pan and Yang 2010). Current approaches transfer farm-level models (Islam Sajol et al 2024; Li et al 2024), without exploiting possible structure in the meteorological inputs. However, identifying this structure and training individual models for each identified weather pattern can improve WPF performance (Rana et al 2016). To the best of our knowledge, these approaches have not yet been used to enable cross-site knowledge transfer.

In this paper, we propose a transfer learning framework that bridges this gap. By investigating whether transfer learning with limited historical data across various European sites can achieve high performance, we thus emulate the constraints of newly commissioned sites. Our model learns domain-agnostic representations of offshore weather across Northern Europe, which can be clustered by meteorological similarity rather than location. Thus, one-hour ahead forecasting models can be trained for each weather condition, and data from target wind farms can be mapped by similarity to an existing meteorological cluster. The relevant model can then be fine-tuned with minimal site-specific data. We present our global methodology in [Figure 1](#).

The remainder of this paper is organised as follows. [Section 2](#) describes the dataset and methodology used. [Section 3](#) presents and analyses the experimental results, for which [Section 4](#) provides further discussion.¹

2. Methodology

2.1. Dataset

We use the offshore wind farm dataset introduced by Grothe et al (2022), which provides meteorological and synthetic power production data on an hourly basis, over 40 years (up to and including 2019) for 29 major European offshore wind farms. The meteorological data is derived from ERA5, a global reanalysis dataset produced by the European Centre for Medium-Range Weather Forecasts that provides consistent hourly estimates of certain atmospheric variables. This data is combined with turbine-specific power curves to generate realistic hourly power production time series for research purposes.

2.2. Selecting Source Wind Farms

To capture a comprehensive representation of meteorological patterns across Northern Europe, source wind farms are selected to maximise meteorological and operational diversity. Exposure to such diversity allows the models to learn from a broader range of atmospheric patterns, enhancing their ability to generalise to new sites that have distinct meteorological characteristics.

¹The full code is available at <https://anonymous.4open.science/r/offshore-wind-forecasting-2026-3EA5/README.md>

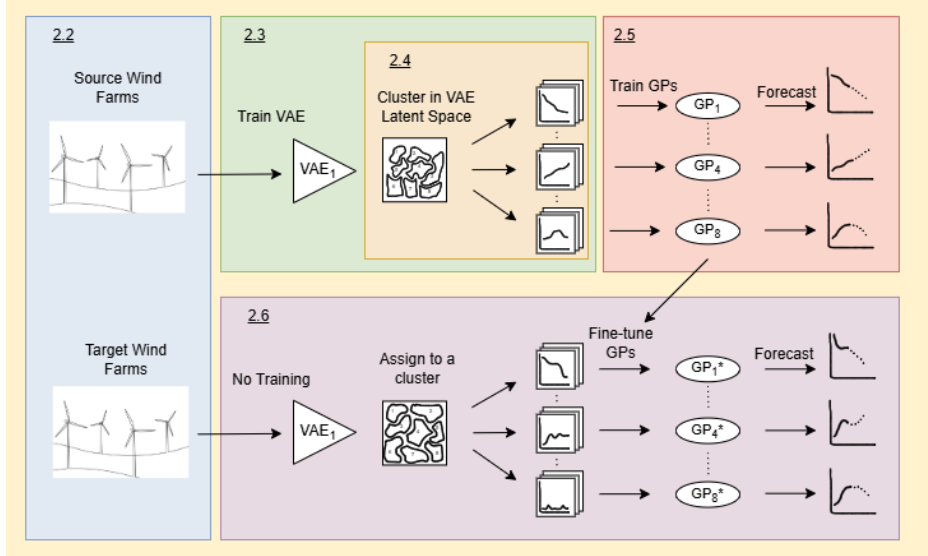
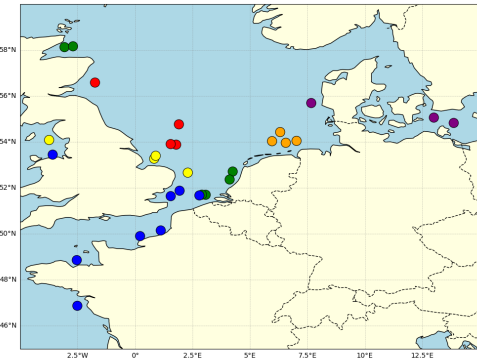


Figure 1: Methodology overview.

For each of the 29 available wind farms, a 38 dimensional vector is extracted from data recorded between January 1, 2018, and December 31, 2019. The feature set included wind speed statistics (mean, variance, percentiles), sea surface roughness distributions, wind directional consistency, power output metrics (including capacity factor and efficiency) and the frequency of extreme weather events. Dimensionality reduction is performed using Uniform Manifold Approximation and Projection (McInnes et al 2020), configured to consider 15 nearest neighbours for each data point and with a minimum distance of 0.1. This is followed by agglomerative hierarchical clustering (Ward 1963), which partitions the farms into six distinct clusters based on both their meteorological and operational profiles. From each cluster, one farm is selected to represent the cluster as a source wind farm.



(a) Distribution of wind farm clusters.



(b) Wind farms selected for source models.

Figure 2: Location and cluster assignment for available wind farms with the selected source wind farms

2.3. Identifying and Clustering Weather Patterns

To identify distinct weather patterns across the six source wind farms, hourly meteorological data from all farms is segmented into continuous, non-overlapping time periods of length p hours. Each period i is represented as a multivariate time-series $\mathbf{X}_i \in \mathbb{R}^{p \times d}$, with $d = 6$ meteorological features: wind speed, sea surface roughness, wind direction components ($\sin \theta$ and $\cos \theta$ for a wind direction θ) and horizontal and vertical wind velocity components at 100m above sea level (u_{100}, v_{100}). To ensure the forecasting models are trained on the most distinct weather patterns, the time-period length p and cluster count K are optimised via grid search, maximising the separation between identified weather patterns (see Section 2.4).

For a fixed time-period length p , we train a Variational Autoencoder (VAE) (Kingma and Welling 2022) to learn a compressed representation of each weather pattern, with the encoder $q_\phi(\mathbf{z} \mid \mathbf{X})$ mapping each input multivariate time-series to an 8-dimensional latent vector $\mathbf{z} \in \mathbb{R}^8$. The architecture contains two 1D convolutional layers with kernel sizes of 5 and 3, designed to extract short-term local features. These feature maps are processed by a Bidirectional Long Short-Term Memory (BiLSTM) network, which captures global temporal dependencies by traversing the sequence in both forward and backward directions (Schuster and Paliwal 1997). The final concatenated hidden states are projected via fully connected layers to parametrise the variational posterior, $\mu_\phi(\mathbf{X}) \in \mathbb{R}^8$ and $\log \sigma_\phi^2(\mathbf{X}) \in \mathbb{R}^8$. Latent variables are subsequently sampled via the reparametrisation trick $\mathbf{z} = \mu_\phi(\mathbf{X}) + \sigma_\phi(\mathbf{X}) \odot \boldsymbol{\varepsilon}$, where $\boldsymbol{\varepsilon} \sim \mathcal{N}(\mathbf{0}, \mathbf{I})$ and \odot denotes element-wise multiplication. The decoder, $p_\theta(\mathbf{X} \mid \mathbf{z})$, performs the inverse reconstruction but employs a unidirectional LSTM for sequence generation. The latent vector \mathbf{z} is first expanded via a fully connected layer and repeated across the temporal dimension p to initialise the sequence. This sequence is processed by the unidirectional LSTM to reconstruct the temporal dynamics, followed by transposed convolutional layers to recover the original multivariate dimensions and local structure of the time-series $\hat{\mathbf{X}}$.

The model parameters θ and ϕ are optimised by minimising the β -VAE loss function (Higgins et al 2017) with mean squared error reconstruction loss and KL divergence regularisation:

$$\mathcal{L}(\theta, \phi; \mathbf{X}) = \mathbb{E}_{q_\phi(\mathbf{z} \mid \mathbf{X})} \left(\|\mathbf{X} - \hat{\mathbf{X}}\|_2^2 \right) + \beta D_{\text{KL}} \left(q_\phi(\mathbf{z} \mid \mathbf{X}) \parallel \mathcal{N}(\mathbf{0}, \mathbf{I}) \right).$$

Training was run for up to 200 epochs using AdamW optimisation (Loshchilov and Hutter 2019). To mitigate posterior collapse, we employ a monotonic annealing schedule for β , linearly increasing from 0.01 to 1.0. For inference, each period was deterministically encoded as the variational posterior mean, $\mathbf{z}_i = \mu_\phi(\mathbf{X}_i)$ providing a concise representation of the meteorological temporal dynamics. The latent vectors are L2-normalised to prioritise directional similarity over magnitude, then partitioned into K distinct weather clusters using Hierarchical Agglomerative clustering with Ward's linkage (Ward 1963) and euclidean distance.

2.4. Optimal Configuration Selection

The optimal configuration (p, K) is selected via grid search by maximising a composite quality score Q . Drawing upon the multi-objective framework of Rana et al (2016), the composite score aggregates six metrics, designed to balance statistical rigour in the latent space with physical interpretability and temporal coherence:

$$Q = 0.2S + 0.2\tilde{D} + 0.2\tilde{C} + 0.25\tilde{M} + 0.1T + 0.05H.$$

Structural quality is evaluated using the Silhouette score S (Rousseeuw 1987), which measures cluster cohesion and separation; the normalised Davies-Bouldin index \tilde{D} (Davies and Bouldin 1979) which evaluates intra-cluster similarity relative to inter-cluster separation; and the normalised Calinski-Harabasz

index \tilde{C} (Caliński and JA 1974) which quantifies the ratio of between cluster to within-cluster dispersion. Physical interpretability is validated using meteorological separability \tilde{M} , calculated as the log-normalised mean ANOVA F-statistic across wind speed, wind variability and power output while robustness is assessed through temporal coherence T , defined as the average within-cluster autocorrelation (Warren Liao 2005), and distributional consistency ($H = 1 - \text{JSD}$), which uses the Jennen-Shannon Divergence (Lin 1991) to penalise shifts in cluster proportions between training and testing sets. As detailed in [Appendix B](#), a sensitivity analysis reveals a trade-off between these objectives: while structural metrics (S, \tilde{D}, \tilde{C}) prefer compact representations with fewer clusters, physical and temporal metrics (\tilde{M}, T) improve with more clusters. The weights in the composite equation were therefore calibrated to negotiate this trade-off.

2.5. Gaussian Process Models

Following the assignment of meteorological periods to the K identified weather clusters, we model the relationship between atmospheric conditions and power generation using cluster-specific Gaussian Process regression (Williams and Rasmussen 2006). For each cluster k , a separate GP $f_k(\mathbf{x}) \sim \mathcal{GP}(m_k(\mathbf{x}), k_k(\mathbf{x}, \mathbf{x}'))$ is trained to learn the cluster-dependent power curve, enabling each model to specialise on the distinct dynamics characterising that specific weather type.

To capture both the overall period trajectory and immediate local conditions, we construct a 20-dimensional input vector $\mathbf{x} \in \mathbb{R}^{20}$ for each hourly forecast. This vector concatenates the 8-dimensional latent representation \mathbf{z} with 12 physical predictors: current wind speed and sea surface roughness; autoregressive lags ($t - 1, t - 2$) for both power and wind speed; and cyclical encodings (\sin, \cos) of the hour, month and wind direction.

The covariance function (kernel) is designed to capture the multi-scale nature of wind power generation across the wind farms. We employ a composite kernel consisting of a Squared Exponential (RBF) component to model smooth power curve trends, summed with a Matérn- $\nu = 3/2$ component to capture the rougher, non-differentiable stochastic fluctuations typical of high-frequency atmospheric turbulence:

$$k_k(\mathbf{x}, \mathbf{x}') = \sigma_{f,k}^2 \left(k_{\text{RBF}}(\mathbf{x}, \mathbf{x}'; \boldsymbol{\ell}_k^{\text{RBF}}) + k_{\text{Matérn}}(\mathbf{x}, \mathbf{x}'; \boldsymbol{\ell}_k^{\text{Mat}}, \nu = 1.5) \right),$$

where $\sigma_{f,k}^2$ controls the output variance. Both components utilise Automatic Relevance Determination (ARD), where $\boldsymbol{\ell}_k \in \mathbb{R}^{20}$ represents a vector of length-scales. This allows the GP to automatically determine the relevance of each input feature for each specific cluster, for example weighting lags more heavily in stable conditions versus turbulence features during storms.

Observation noise is modelled via a Gaussian likelihood with variance $\sigma_{n,k}^2$, assuming $y = f_k(\mathbf{x}) + \varepsilon$ where $\varepsilon \sim \mathcal{N}(0, \sigma_{n,k}^2)$. Consequently, the covariance of the noisy observations is given by $\mathbf{K}_{y,k} = k_k(\mathbf{x}, \mathbf{x}') + \sigma_{n,k}^2 I$. The complete hyperparameter set $\theta_k = \{\sigma_{f,k}^2, \sigma_{n,k}^2, \boldsymbol{\ell}_k^{\text{RBF}}, \boldsymbol{\ell}_k^{\text{Mat}}, c_k\}$ is optimised by maximising the exact Marginal Log-Likelihood (MLL) of the observations. Using the noisy covariance $\mathbf{K}_{y,k}$, the MLL is defined as:

$$\log p(\mathbf{y} | X, \theta_k) = -\frac{1}{2}(\mathbf{y}^\top \mathbf{K}_{y,k}^{-1} \mathbf{y}) - \frac{1}{2} \log |\mathbf{K}_{y,k}| - \frac{N}{2} \log(2\pi).$$

2.6. Transfer Learning

To evaluate the cross-site generalisation capability of the proposed framework, we apply a transfer learning strategy where the library of GP models are adapted to eight unseen target farms. This adaptation utilises the fixed VAE encoder ϕ_S and the set of cluster-specific GP priors, proceeding in three stages: latent projection, cluster alignment and GP fine-tuning. First, the target meteorological time series \mathbf{X}_t

are projected into the source latent space using the fixed source encoder $\mathbf{z}_T = \mu_{\phi_S}(\mathbf{X}_T)$. This enforces that target weather patterns are interpreted through the learned representation of the source domain. Each target period is then assigned to one of the K source weather clusters via a nearest-neighbourhood classification in the latent space, utilising the centroid from the source training set.

For each identified weather pattern $c \in \{1, \dots, k\}$, we initialise a target GP $f_T^{(c)}$ using the hyperparameters of the corresponding source GP, $f_S^{(c)}$. This initialisation provides a strong prior on the temporal covariance structure of the power output. The kernel hyperparameters θ_k are then optimised by maximising the exact marginal log-likelihood on the available target training data $\mathcal{D}_{\text{train}}$:

$$\hat{\theta}_T = \underset{\theta}{\operatorname{argmax}} \log p(\mathbf{y}_{\text{train}} \mid \mathbf{X}_{\text{train}}, \theta, \sigma_{n, \text{fixed}}^2). \quad (2.1)$$

To assess data efficiency, we conducted experiments varying the data availability of the two-year target datasets. Each target dataset is split into training fractions $\gamma \in \{0.1, 0.2, 0.3, 0.4, 0.5\}$, simulating a ‘cold start’ scenario where a newly commissioned wind farm has been operational for only a short period (ranging from approximately 2.4 to 12 months). The remaining $1 - \gamma$ is reserved for testing.

3. Results

To evaluate the performance of our transfer framework under each data availability scenario, we benchmark our results against a baseline of cluster-specific GPs trained from scratch, representing the standard no-transfer approach. We assess the accuracy of these models using Mean Absolute Error (MAE), Root Mean Square Error (RMSE) and the coefficient of determination (R^2), as recalled in [Appendix A](#). To ensure comparability across wind farms, MAE is expressed as a percentage of total capacity, while aggregated results are weighted by the number of time-periods in each cluster to account for varying cluster sizes. The six-hour time window with $K = 8$ clusters was identified as the best configuration, with a composite score of $Q = 0.53$ (averaged for random seeds 42, 63, 84). This setting provides the most effective trade-off between intra-cluster cohesion and the differentiation of meteorological patterns. The resulting structural separation is visualised in Figure 3, where the 8-dimensional latent representations are embedded into a two-dimensional plane using t-SNE (Maaten and Hinton [2008](#)). Figure 4 validates the physical distinctiveness via mean wind speed distributions. Clusters 1 and 5 capture calm periods, while cluster 2 isolates high-speed extremes. In contrast, cluster 0 exhibits higher internal variance, likely characterising transitional atmospheric states.

3.1. Quantitative Results

The library of GP models achieved an overall MAE of $3.68\% \pm 0.04\%$ (24.4MW; RMSE=42.0MW; $R^2 = 0.981$) when evaluated using two years of operational data across the six source farms (4:1 split; averaged over seeds 42, 63, 84). The distinct performance variation across clusters, as seen in [Table 1](#), and the variability conditioned on farm location, as seen in [Figure 5](#), validates the pooling of source data across farm sites. By capturing a comprehensive distribution of wind behaviours, the models learn a robust representation of intra-cluster variations, thereby facilitating quicker adaptation to the specific conditions of target wind farms.

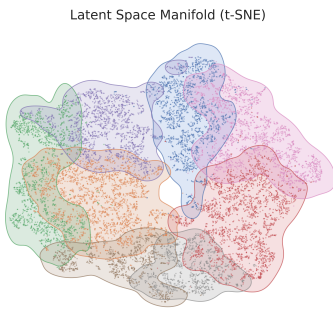


Figure 3: Latent space manifold visualised via t-SNE, showing the distribution of training periods across weather clusters.

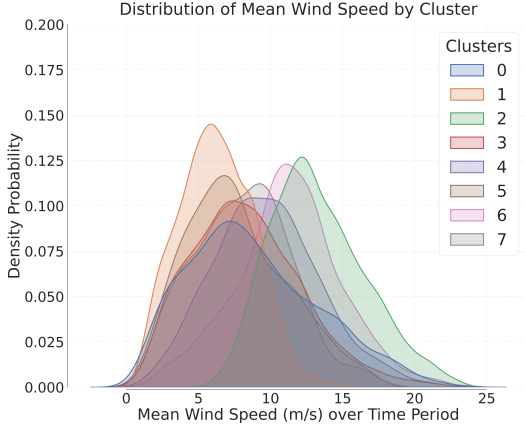


Figure 4: Mean wind speed distribution of training periods by cluster (exemplified by seed 84).

Cluster	Test samples	MAE (%)	
		GP	RF
0	2682	3.93	4.26
1	2845	3.38	3.73
2	2110	3.32	3.47
3	2228	3.76	4.14
4	2187	3.97	4.26
5	2170	3.44	3.78
6	1290	3.90	4.31
7	1312	3.78	4.07
Overall	17,490	3.68	4.00

Table 1: Cluster-level performance of GP and RF models averaged across 3 seeds.

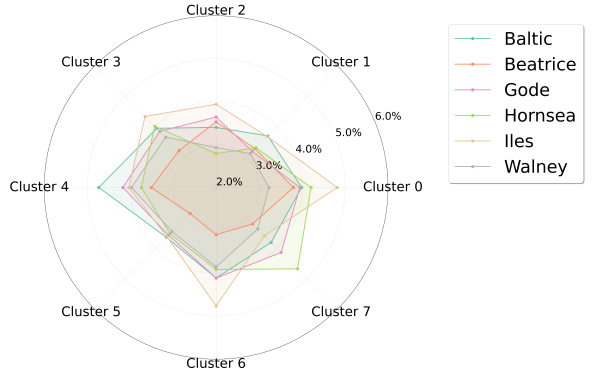


Figure 5: Performance of GP forecasts, disaggregated by wind farm and cluster.

The transfer learning performance of each cluster and data capacity, as shown in Table 2, are averaged across the eight target farms and three random seeds per farm (breakdown of baseline results are provided in [Appendix C](#)). The results demonstrate the proposed framework’s superior generalisation capability compared to training individual forecasting models, significantly reducing the data requirements for offshore WPF. With under five months of local data (20% data capacity), the framework achieves an average MAE of 3.52% (26.7 MW). This represents a 14.7% improvement in raw MAE over the baseline (4.13%; 31.3 MW) and outperforms the baseline models even when trained on a full year of data. The results also show how transferability varies by meteorological condition. Some clusters generalise quickly to new sites, such as cluster 1, which achieves an MAE of 3.7% with approximately 2.4 months of data. In contrast, cluster 7 requires more site-specific tuning, yielding an MAE of 5.8% with approx 2.4 months of data, which improves to 3.4% with approx 7.2 months. This suggests that while the source GPs encode the general structure of these weather patterns, cluster 7’s phenomena are more location-dependent, necessitating a large volume of local data for effective fine-tuning.

Table 2: Transfer learning performance by Cluster and Data Capacity aggregated across all 8 target farms.

Clusters	Data Capacity									
	10%		20%		30%		40%		50%	
	MAE (%)	R^2	MAE (%)	R^2	MAE (%)	R^2	MAE (%)	R^2	MAE (%)	R^2
0	4.4	0.96	3.7	0.97	3.5	0.97	3.5	0.97	3.5	0.97
1	3.7	0.95	3.3	0.96	3.2	0.96	3.2	0.96	3.1	0.96
2	3.9	0.85	3.2	0.89	3.0	0.91	2.9	0.91	2.9	0.91
3	4.5	0.96	3.7	0.97	3.3	0.98	3.2	0.98	3.2	0.98
4	5.1	0.94	3.9	0.97	3.5	0.97	3.4	0.97	3.4	0.97
5	4.5	0.94	3.6	0.95	3.2	0.96	3.1	0.97	3.1	0.97
6	4.8	0.92	3.7	0.96	3.4	0.96	3.3	0.96	3.3	0.96
7	5.8	0.83	3.8	0.93	3.4	0.94	3.2	0.95	3.1	0.95
Average	4.34%	0.933	3.52%	0.956	3.30%	0.960	3.23%	0.963	3.22%	0.963
Baseline Average	5.26%	0.911	4.13%	0.945	3.74%	0.953	3.59%	0.957	3.55%	0.959

3.2. Farm-specific Analysis

Breaking down performance by individual target site reveals how transferability varies according to the specific meteorological conditions unique to each farm. As shown in Table 3 for the Gemini wind farm, Clusters 0, 1, 2, 3, and 7 exhibit particularly strong transferability. In these regimes, the pre-trained GP models align well with local dynamics, all yielding MAEs below 3.4% with approximately five months of fine-tuning data. Crucially, these clusters represent 66.7% of the evaluated time periods (at 20% data capacity), underscoring the substantial operational benefit of the framework. Conversely, Clusters 4, 5, and 6 demonstrate lower transferability; this suggests that their associated weather patterns are more distinct to the Gemini location, necessitating additional local data to refine the representations learned by the GPs.

Table 3: Transfer learning performance by Cluster and Data Capacity for the Gemini Wind Farm.

Clusters	Test Samples at 20% capacity	Data Capacity				
		10%	20%	30%	40%	50%
		MAE (%)	MAE (%)	MAE (%)	MAE (%)	MAE (%)
0	1788	4.3	3.3	3.1	3.3	3.0
1	2095	4.2	3.4	3.3	3.3	3.2
2	1492	2.4	2.2	2.2	2.1	1.9
3	1448	4.3	3.4	3.1	3.2	3.1
4	1358	5.5	4.4	3.8	3.6	3.4
5	1223	5.5	3.9	3.6	3.4	3.5
6	1333	6.7	4.2	3.6	3.4	3.5
7	922	4.4	2.7	2.7	2.6	2.5
Average		4.29%	3.31%	3.10%	3.06%	2.98%
Baseline Average		5.06%	3.90%	3.53%	3.35%	3.31%

4. Discussion

The proposed framework demonstrates that weather-specific transfer learning significantly reduces data requirements for accurate forecasting in European offshore wind farms. To scale this approach, future work will establish geographic transfer clusters across diverse climate zones. Furthermore, incorporating turbine specifications and wake effect modelling will account for intra-farm turbine heterogeneity. Collectively, these advancements pave the way toward a dynamic WRA tool capable of generating rapid, location- and configuration-specific forecasts without the need for lengthy initial data investment, thus paving the way for future investments into offshore wind farms, and allowing the growth of cheaper, greener energy.

References

Ally S, Verstraeten T, Daems PJ, Nowé A and Helsen J (2025) Modular deep learning approach for wind farm power forecasting and wake loss prediction. *Wind Energy Science* **10**(4), 779–812. doi: [10.5194/wes-10-779-2025](https://doi.org/10.5194/wes-10-779-2025). <https://doi.org/10.5194/wes-10-779-2025>.

Caliński T and JA H (1974) A Dendrite Method for Cluster Analysis. *Communications in Statistics - Theory and Methods* **3**, 1–27. doi: [10.1080/03610927408827101](https://doi.org/10.1080/03610927408827101).

Davies DL and Bouldin DW (1979) A Cluster Separation Measure. *IEEE Transactions on Pattern Analysis and Machine Intelligence* **PAMI-1**, 224–227. <https://api.semanticscholar.org/CorpusID:13254783>.

Ember Energy (2025) Offshore wind targets underpin acceleration to 2030 and beyond. Available at <https://ember-energy.org/latest-insights/offshore-wind-targets-underpin-acceleration-to-2030-and-beyond/>.

ESMAP (2019) tech. rep. Going Global: Expanding Offshore Wind to Emerging Markets. World Bank Group and Energy Sector Management Assistance Program (ESMAP). Available at <https://documents.worldbank.org/curated/en/716891572457609829/pdf/Going-Global-Expanding-Offshore-Wind-To-Emerging-Markets.pdf>.

Global Wind Energy Council (2025) tech. rep. Global Wind Report 2025. Global Wind Energy Council. Available at <https://www.gwec.net/reports/globalwindreport>.

Grothe O, Kächele F and Watermeyer M (2022) Analyzing Europe's Biggest Offshore Wind Farms: A Data Set with 40 Years of Hourly Wind Speeds and Electricity Production. *Energies* **15**(5). issn: 1996-1073. doi: [10.3390/en15051700](https://doi.org/10.3390/en15051700). <https://doi.org/10.3390/en15051700>.

Higgins I, Matthey L, Pal A, Burgess C, Glorot X, Botvinick M, Mohamed S and Lerchner A (2017) beta-VAE: Learning Basic Visual Concepts with a Constrained Variational Framework. In *International Conference on Learning Representations*. Available at <https://openreview.net/forum?id=Sy2fzU9gl>.

Islam Sajol MS, Shazid Islam M, Jahid Hasan ASM, Saydur Rahman M and Yusuf J (2024) Wind Power Prediction across Different Locations using Deep Domain Adaptive Learning. In *2024 6th Global Power, Energy and Communication Conference (GPECOM)*, 518–523. doi: [10.1109/GPECOM51896.2024.10582569](https://doi.org/10.1109/GPECOM51896.2024.10582569).

Kingma DP and Welling M (2022) *Auto-Encoding Variational Bayes*. arXiv: [1312.6114 \[stat.ML\]](https://arxiv.org/abs/1312.6114). Available at <https://arxiv.org/abs/1312.6114>.

Li D, Hu Y, Yang B, Fang Z, Liang Y and He S (2024) A novel transfer learning strategy for wind power prediction based on TimesNet-GRU architecture. *Journal of Renewable and Sustainable Energy* **16**. doi: [10.1063/5.0200518](https://doi.org/10.1063/5.0200518).

Lin J (1991) Divergence measures based on the Shannon entropy. *IEEE Transactions on Information Theory* **37**(1), 145–151. doi: [10.1109/18.61115](https://doi.org/10.1109/18.61115).

Loshchilov I and Hutter F (2019) *Decoupled Weight Decay Regularization*. arXiv: [1711.05101 \[cs.LG\]](https://arxiv.org/abs/1711.05101). Available at <https://arxiv.org/abs/1711.05101>.

Maaten L van der and Hinton G (2008) Visualizing Data using t-SNE. *Journal of Machine Learning Research* **9**(86), 2579–2605. <http://jmlr.org/papers/v9/vandermaaten08a.html>.

McInnes L, Healy J and Melville J (2020) *UMAP: Uniform Manifold Approximation and Projection for Dimension Reduction*. arXiv: [1802.03426 \[stat.ML\]](https://arxiv.org/abs/1802.03426). Available at <https://arxiv.org/abs/1802.03426>.

Pan SJ and Yang Q (2010) A Survey on Transfer Learning. *IEEE Transactions on Knowledge and Data Engineering* **22**(10), 1345–1359. doi: [10.1109/TKDE.2009.191](https://doi.org/10.1109/TKDE.2009.191).

Rana M, Koprinska I and Agelidis V (2016) Solar Power Forecasting Using Weather Type Clustering and Ensembles of Neural Networks. In doi: [10.1109/IJCNN.2016.7727853](https://doi.org/10.1109/IJCNN.2016.7727853).

Rousseeuw PJ (1987) Silhouettes: a graphical aid to the interpretation and validation of cluster analysis. *Journal of Computational and Applied Mathematics*.

Schuster M and Paliwal K (1997) Bidirectional recurrent neural networks. *IEEE Transactions on Signal Processing* **45**(11), 2673–2681. doi: [10.1109/78.650093](https://doi.org/10.1109/78.650093).

Statista (2025) Number of offshore wind farms worldwide as of April 2025, by country. Available at <https://www.statista.com/statistics/264257/number-of-offshore-wind-farms-worldwide-by-country/>.

Ward JH (1963) Hierarchical Grouping to Optimize an Objective Function. *Journal of the American Statistical Association* **58**(301), 236–244. issn: 01621459, 1537274X. <http://www.jstor.org/stable/2282967>.

Warren Liao T (2005) Clustering of time series data—a survey. *Pattern Recognition* **38**(11). issn: 0031-3203. doi: <https://doi.org/10.1016/j.patcog.2005.01.025>. <https://www.sciencedirect.com/science/article/pii/S0031320305001305>.

Williams CK and Rasmussen CE (2006) *Gaussian Processes for Machine Learning*. vol 2. 3. MIT press Cambridge, MA. Available at <https://doi.org/10.7551/mitpress/3206.001.0001>.

A. Metrics Used

Model performance is assessed using three complementary metrics standard in the WPF literature and in the forecasting literature more generally.

Mean Absolute Error

The Mean Absolute Error (MAE) quantifies the average magnitude of prediction errors without considering direction:

$$\text{MAE} = \frac{1}{n} \sum_{i=1}^n |y_i - \hat{y}_i|$$

where y_i denotes the observed values output and \hat{y}_i denotes the predicted values.

Root Mean Square Error

The Root Mean Square Error (RMSE) measures the square root of the average of the squared differences between prediction and observed value. Unlike MAE, RMSE gives a relatively higher weight to large errors:

$$\text{RMSE} = \sqrt{\frac{1}{n} \sum_{i=1}^n (y_i - \hat{y}_i)^2}$$

where y_i denotes the observed values output and \hat{y}_i denotes the predicted values.

Coefficient of Determination

The Coefficient of Determination (R^2) quantifies the proportion of variance in the observed data explained by the model:

$$R^2 = 1 - \frac{\sum_{i=1}^n (y_i - \hat{y}_i)^2}{\sum_{i=1}^n (y_i - \bar{y})^2}.$$

where y_i denotes the observed values output, \hat{y}_i denotes the predicted values and \bar{y} denotes the mean of the observed values.

B. Optimal Configuration Selection

To validate the robustness of the composite quality score Q , we performed a sensitivity analysis evaluating the impact of the time-period length, p , and number of clusters, K , on each constituent metric independently. This sensitivity analysis breaks down the contributions of each metric to the final composite score.

Table 4: Performance of cluster size and time period length configurations across each composite score metric.

(a) Only Silhouette Score							(b) Only Meteorological Separability						
Time Period	8	10	Clusters		14	16	Time Period	8	10	Clusters		14	16
6	0.168	0.143	0.132	0.137	0.129		6	0.536	0.563	0.562	0.576	0.585	
12	0.190	0.175	0.160	0.143	0.136		12	0.512	0.512	0.504	0.520	0.515	
24	0.168	0.153	0.145	0.138	0.133		24	0.427	0.437	0.439	0.442	0.440	
36	0.147	0.133	0.124	0.126	0.128		36	0.377	0.376	0.385	0.386	0.386	
48	0.162	0.152	0.147	0.149	0.144		48	0.377	0.370	0.392	0.387	0.379	

(c) Only Davies-Bouldin Index							(d) Only Temporal Coherence						
Time Period	8	10	Clusters		14	16	Time Period	8	10	Clusters		14	16
6	0.237	0.207	0.206	0.216	0.236		6	0.782	0.813	0.819	0.826	0.834	
12	0.193	0.219	0.216	0.194	0.206		12	0.713	0.720	0.737	0.757	0.766	
24	0.169	0.167	0.187	0.183	0.200		24	0.592	0.625	0.650	0.667	0.685	
36	0.174	0.165	0.187	0.184	0.197		36	0.554	0.564	0.581	0.595	0.603	
48	0.198	0.192	0.205	0.213	0.238		48	0.492	0.511	0.545	0.561	0.574	

(e) Only Calinski-Harabasz							(f) Distribution Consistency						
Time Period	8	10	Clusters		14	16	Time Period	8	10	Clusters		14	16
6	0.933	0.919	0.909	0.902	0.894		6	0.998	0.998	0.997	0.998	0.997	
12	0.842	0.829	0.820	0.811	0.803		12	0.998	0.997	0.996	0.995	0.994	
24	0.766	0.752	0.740	0.731	0.724		24	0.998	0.997	0.997	0.996	0.995	
36	0.708	0.695	0.683	0.676	0.670		36	0.993	0.992	0.992	0.992	0.992	
48	0.703	0.690	0.678	0.669	0.662		48	0.996	0.995	0.994	0.995	0.994	

C. Baseline Results

These results illustrate the baseline forecasting performance, stratified by cluster and data capacity, aggregated across all eight target wind farms and three random seeds (42, 63, 84).

Table 5: Baseline Performance by Cluster and Data Capacity

Clusters	Data Capacity											
	10%		20%		30%		40%		50%			
	MAE (%)	R^2	MAE (%)	R^2	MAE (%)	R^2	MAE (%)	R^2	MAE (%)	R^2	MAE (%)	R^2
0	5.3	0.94	4.4	0.96	4.0	0.97	3.9	0.97	3.9	0.97	3.9	0.97
1	4.5	0.93	3.8	0.95	3.5	0.96	3.5	0.96	3.4	0.96	3.4	0.96
2	4.6	0.81	3.7	0.88	3.4	0.89	3.2	0.90	3.2	0.90	3.2	0.91
3	5.5	0.95	4.4	0.96	3.8	0.97	3.6	0.97	3.7	0.97	3.7	0.97
4	6.0	0.93	4.6	0.96	4.1	0.97	3.9	0.97	3.9	0.97	3.9	0.97
5	5.6	0.90	4.2	0.94	3.7	0.95	3.5	0.96	3.5	0.96	3.5	0.96
6	5.7	0.90	4.3	0.94	3.9	0.95	3.6	0.96	3.6	0.96	3.6	0.96
7	7.5	0.78	4.6	0.91	4.1	0.92	3.7	0.94	3.5	0.94	3.5	0.94
Average	5.26%	0.911	4.13%	0.945	3.74%	0.953	3.59%	0.957	3.55%	0.959		